J. Fluid Mech. (2022), *vol*. 936, A30, doi:10.1017/jfm.2022.25

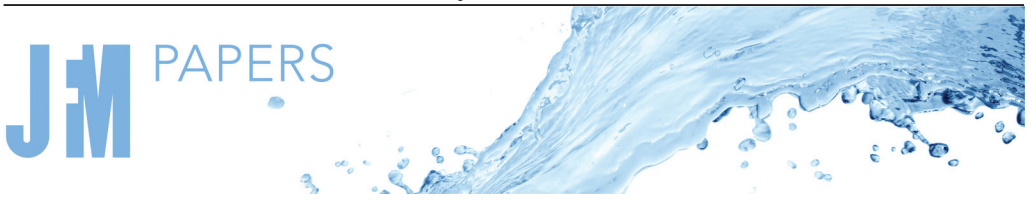

On the direction of the re-entrant jet and the limiting cavity flow configurations

Dmitri V. Maklakov[1],† **and Anna I. Lexina**[1]

[1]N.I. Lobachevsky Institute of Mathematics and Mechanics, Kazan (Volga region) Federal University, Kremlyovskaya 35, Kazan 420008, Russia

(Received 10 May 2021; revised 2 October 2021; accepted 8 January 2022)

In this paper, we investigate an old classical free streamline problem, namely, the two-dimensional re-entrant jet cavity flow past an obstacle. It is well known that for the re-entrant jet model, the direction of the jet is a free parameter that can be specified arbitrarily. To fix this uncertainty, we make a complementary conjecture: the direction should be chosen so that the mean kinetic energy of the remote part of the jet is minimal. Considering cavity flows over an oblique flat plate as an example, we show numerically that the direction is almost opposite to the incident flow. In addition, we present an analytical confirmation of this conclusion that is independent of the obstacle shape. Further, considering again the oblique flat plate as an example, we give an answer to the following question: What happens when the angle of attack tends to zero and the cavity number is finite? We demonstrate that for the limiting configurations, the re-entrant jet vanishes, and the limit is a free-surface flow with a symmetric bubble above the plate and two stagnation points on the lower side of the plate. For this limit we construct a simple exact analytical solution.

Key words: cavitation, jets, separated flows

1. Introduction

In the last two decades, numerical methods for studying cavitation flows based on Reynolds averaged Navier–Stokes equations (RANSE) are rapidly developing (see e.g. Niedzwiedzka, Schnerr & Sobieski 2016). Despite this, potential models for studying cavitation phenomena do not lose their significance. Consider, for example, the work by Vernengo *et al.* (2016), where the optimal shapes of two-dimensional supercavitating hydrofoils are found using the potential-based panel method (Kinnas & Fine 1991), and then the results are verified using a high-precision non-stationary multiphase viscous solver (Bonfiglio & Brizzolara 2016). However, in the study of cavitation flows, panel

† Email address for correspondence: dmaklak@kpfu.ru

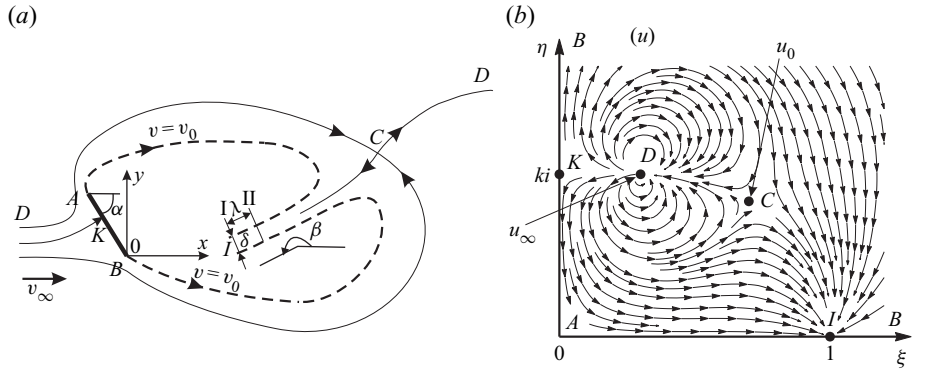

Figure 1. (*a*) Sketch of the steady two-dimensional re-entrant jet cavity flow over an oblique flat plate. (*b*) The domain in the parametric u-plane together with the streamlines.

methods, even applied to the two-dimensional case, require an iterative procedure to determine the shape of the interface between the gas and liquid phases. When studying two-dimensional cavitation flows over polygonal obstacles, the need for such a procedure completely disappears if the method of conformal mappings is applied. Despite the large number of works devoted to the development of this method, there are problems that have not been fully investigated. One of them is a supercavitating re-entrant flow over an inclined flat plate.

The steady potential re-entrant jet cavity model was proposed independently by Efros (1946) and Kreisel (1946). The model is characterized by the presence of a stagnation point in the cavity closure region and by formation of an infinitely long re-entrant jet that is continued mathematically into a second Riemann sheet. A sketch of the re-entrant jet flow over an oblique flat plate is shown in figure 1(*a*). The model is described in all classical and modern books devoted to studies of the cavitation phenomenon (see, e.g. Birkhoff & Zarantonello 1957; Gilbarg 1960; Gurevich 1965; Brennen 1995; Franc & Michel 2004; Terentiev, Kirschner & Uhlman 2011).

Gilbarg & Serrin (1950) carried out a general mathematical investigation of the model and deduced elegant formulae for the lift and drag forces, L and D:

$$L = -Q\rho v_0 \sin\beta - \rho v_\infty \Gamma, \quad D = -Q\rho v_0 \cos\beta + \rho v_\infty Q, \tag{1.1a,b}$$

which are correct for a curved plate of any shape. In (1.1), ρ is the density of the fluid, v_∞ is the incident velocity, v_0 is the constant fluid velocity along the cavity boundaries, Γ is the circulation around the body–cavity system, Q is the flow flux in the re-entrant jet, and β is the angle of inclination of the re-entrant jet with respect to the incident flow direction.

Numerous experiments show that due to the impingement of upper and lower flows behind the body, the re-entrant jet really forms in the cavity closure region, periodically disperses, and runs away into the main stream. So, between the re-entrant jet in real three-dimensional cavity flows (see e.g. Karn, Arndt & Hong 2016) and that shown in figure 1(*a*), there is only formal resemblance. The re-entrant jet is only one of the possible ways of organizing the potential flow in the cavity closure region with all deficiencies inherent to all potential models of supercavitation. Indeed, the flow in the cavity closure region is turbulent and essentially unsteady, so it cannot be modelled, in principle, in the framework of potential models. This leads to different artificial methods of closing the cavity, which in turn leads to mathematical deficiencies. One of these deficiencies is mathematical indeterminacy: as a rule, the number of accessory parameters

occurring in the process of solving is less than that of physically founded conditions for their determination. For example, for the generalized Riabouchinsky cavity model, the shape of the artificial body closing the cavity can be chosen arbitrarily; for the Joukowski–Roshko–Eppler model with artificial parallel walls (Wu 1956; Mimura 1958) and for the Wu model (Wu 1962) with artificial congruent streamlines, one mathematical parameter turns out to be indefinite; for the Tulin double spiral vortex model (Tulin 1964), the number of the superfluous parameters already equals two. The only cavity model that does not have such a drawback is the Tulin single spiral vortex model with the modification suggested by Terent'ev (1976) (see also Terentiev *et al.* 2011).

Thus, to get a closed system of equations with respect to the accessory parameters, different heuristic artificial conditions are involved. A review of all cavity models reported to date can be found in Terentiev *et al.* (2011).

As to the re-entrant jet model, here, the direction of the jet is an undefined parameter that can be chosen arbitrarily. To have a closed system of equations, Gilbarg & Serrin (1950) suggested specifying the circulation around the body–cavity system. Following this, DeLillo, Elcrat & Hu (2005) computed several examples of re-entrant jet flows over obstacles of different shapes, but the authors did not make any analysis of the influence of the circulation on the hydrodynamic properties. In the second edition of the book by Gurevich (1979), the computations over an oblique flat plate were carried out under the assumption that the re-entrant jet is directed opposite to the incident flow ($\beta = \pi$). Terentiev *et al.* (2011, p. 53) calculated several examples of the re-entrant cavity flow over an oblique flat plate under the same assumption.

As has been mentioned already, the re-entrant jet occurs due to the impact of the upper and lower flows in the vicinity of the cavity closure region. So a part of the kinetic energy of the impinging flows is spent in the formation of the jet. To find the inclination angle β of the re-entrant jet, we put forward the following heuristical principle: the direction of the jet should be chosen so that the average kinetic energy K of the remote part of the jet is minimal. Thus we assume that the flow self-organizes in such a way as to minimize the expenditure of energy for the re-entrant jet formation.

An analogous uncertainty appears in the problem of the oblique impact of two jets of different widths: the directions of one of the outgoing jets turns out to be indefinite (see e.g. Birkhoff & Zarantonello 1957; Gurevich 1965; Milne-Thomson 1968). It seems that Palatini (1916) was the first to apply an energy criterion for fixing such an uncertainty.

One of the most important dimensionless parameters that characterize cavity flows is the cavitation number

$$\sigma = \frac{p_\infty - p_0}{\rho v_\infty^2/2} = \frac{v_0^2}{v_\infty^2} - 1, \tag{1.2}$$

where p_∞ and p_0 are the pressures at the incident flow and inside the cavity, respectively.

As an example of application of the energy conjecture, we consider the cavity flow over an oblique flat plate and demonstrate that the principle gives a quite definite direction of the re-entrant jet for any angle of attack α and any positive cavity number σ. Moreover, in the range of $\sigma \in (0, 1]$, the re-entrant jet direction, defined by the principle, almost coincides with the direction that is opposite to the incident flow. The difference between the two directions is less or slightly higher than one degree, and the corresponding hydrodynamic properties, such as the lift, drag and moment coefficients, agree with each other at least up to four decimal places. This fact allows us to use the assumption made by Gurevich (1979) and Terentiev *et al.* (2011): the direction of the re-entrant jet should be opposite to the incident flow. Since the result $\beta \approx \pi$ is independent of the angle of attack α, we believe

that the same will be true for a curved plate of any shape. This last conclusion has been confirmed by approximate analytical formulae that are based on assumptions independent of the obstacle shape.

Studying systematically the re-entrant jet flows over oblique flat plates, we have established that there exists a range of angles of attack $\alpha \in (0, \alpha_1)$ at which the lift force L increases as the angle of attack α decreases, i.e. $\mathrm{d}C_L/\mathrm{d}\alpha < 0$ for $\alpha \in (0, \alpha_1)$, where C_L is the lift coefficient. An analogous range was found in the monograph by Terentiev *et al.* (2011, figure 2.3.4) for the Tulin single spiral vortex model, but the authors did not consider the limiting passage $\alpha \to 0$. In the present paper, this passage has been investigated numerically. So we give an answer to the following question, which has never been studied before: What happens when the angle of attack α tends to zero and the cavity number σ is finite? We demonstrate that for the limiting configurations, the re-entrant jet vanishes, and the limit is a free-surface flow with a symmetric bubble above the plate and two stagnation points on the lower side of the plate. For this limit we construct a simple exact analytical solution.

2. Mathematical formulation of the problem

Consider a two-dimensional re-entrant jet flow over an oblique flat plate (see figure 1*a*). The origin of the Cartesian coordinate system is located at the trailing edge B, and the incident flow is parallel and co-directional with the x-axis. The flow is assumed to be steady and irrotational, and gravity and capillary forces are neglected. The length of the plate l, the incident velocity v_∞, the angle of attack α and the cavity number σ, defined by (1.2), are assumed to be given.

Let $w = \varphi + \mathrm{i}\psi$ be the complex potential of the flow. We map conformally the flow region in the physical plane $z = x + \mathrm{i}y$ onto the upper right quadrant in the parametric plane $u = \xi + \mathrm{i}\eta$. Under the conformal mapping, the streamlines in the physical z-plane transform to the streamlines in the parametric u-plane shown in figure 1(*b*). In this figure, the points $u = 0, \infty, \mathrm{i}k, 1, u_\infty, u_0$ are, respectively, the images of the leading edge A, trailing edge B, stagnation point K, infinity I of the re-entrant jet, infinity D of the main stream, and the stagnation point C in the cavity closure region.

Making use of Chaplygin's singular point method (see Gurevich 1965), we find that

$$\frac{\mathrm{d}w}{\mathrm{d}u} = l_0 v_0 f(u), \quad f(u) = \frac{u(u^2+k^2)(u^2-u_0^2)(u^2-\overline{u_0}^2)}{(1-u^2)(u^2-u_\infty^2)^2(u^2-\overline{u_\infty}^2)^2}, \tag{2.1a,b}$$

where the overbars mean the complex conjugate values, $v_0 = v_\infty/\sqrt{1+\sigma}$ is the known constant velocity on the boundary of the cavity, and l_0 is an unknown positive constant, which has the dimension of length.

Taking into account that

$$\left|\frac{\mathrm{d}w}{v_0\,\mathrm{d}z}\right|_{u=\xi} = 1, \quad \mathrm{Im}\left(\mathrm{e}^{-\mathrm{i}\alpha}\frac{\mathrm{d}w}{v_0\,\mathrm{d}z}\right)_{u=\mathrm{i}\eta} = 0, \tag{2.2a,b}$$

and applying Chaplygin's method to the complex conjugate velocity, we get

$$\frac{\mathrm{d}w}{v_0\,\mathrm{d}z} = \mathrm{e}^{\mathrm{i}\alpha}F(u), \quad F(u) = \frac{(u-\mathrm{i}k)(u-u_0)(u+\overline{u_0})}{(u+\mathrm{i}k)(u-\overline{u_0})(u+u_0)}. \tag{2.3a,b}$$

Equations (2.1) and (2.3) give a general solution to the problem, and all features of the flow can be determined completely in terms of l_0, $f(u)$ and $F(u)$. In particular, the

derivative $\mathrm{d}z/\mathrm{d}u$ of the function $z(u)$ that maps the parametric u-plane onto the physical z-plane is

$$\frac{\mathrm{d}z}{\mathrm{d}u} = l_0\,\mathrm{e}^{-\mathrm{i}\alpha}\,G(u), \quad G(u) = \frac{f(u)}{F(u)} = \frac{u(u+\mathrm{i}k)^2(u+u_0)^2(u-\overline{u_0})^2}{(1-u^2)(u^2-u_\infty^2)^2(u^2-\overline{u_\infty}^2)^2}. \tag{2.4a,b}$$

Let us introduce the notations

$$u_\infty = a + \mathrm{i}b, \quad u_0 = c + \mathrm{i}d. \tag{2.5a,b}$$

As one can see, (2.1)–(2.4) contain six unknown real accessory parameters: l_0, a, b, c, d and k. To determine these parameters, one needs to deduce six equations. Since the length l of the plate is given, integrating (2.4a) along the imaginary η-axis yields

$$l = l_0\,J(a, b, c, d, k), \tag{2.6}$$

where

$$J = \int_0^\infty G_1(\eta)\,\mathrm{d}\eta, \quad G_1(\eta) = \frac{\eta(\eta+k)^2[(\eta+d)^2+c^2]^2}{(\eta^2+1)[\eta^4+2(a^2-b^2)\eta^2+(a^2+b^2)^2]^2}. \tag{2.7a,b}$$

Equation (2.6) allows us to express l_0 in terms of a, b, c, d and k, namely, $l_0 = l/J$.

Now we deduce equations that do not contain l_0. At the point $u = u_\infty$, the complex conjugate velocity equals v_∞. Taking into account (2.3) and (2.5), we have

$$\frac{[a+\mathrm{i}(b-k)][a-c+\mathrm{i}(b-d)][a+c+\mathrm{i}(b-d)]}{[a+\mathrm{i}(b+k)][a-c+\mathrm{i}(b+d)][a+c+\mathrm{i}(b+d)]} - R\,\mathrm{e}^{-\mathrm{i}\alpha} = 0, \tag{2.8}$$

where

$$R = \frac{v_\infty}{v_0} = \frac{1}{\sqrt{1+\sigma}}. \tag{2.9}$$

Since (2.8) is written in complex form, it contains two real-valued equations.

One more complex-valued equation is obtained from a so-called closure condition that implies the possibility of surrounding the body–cavity system by a closed contour. The latter means that in the expansion of the function $\mathrm{d}z/\mathrm{d}u$ in the vicinity of the point u_∞, the coefficient of the term $(u-u_\infty)^{-1}$ vanishes. Therefore, the residue of the function $G(u)$ at this point is zero:

$$\operatorname*{res}_{u=u_\infty} G(u) = 0, \quad \text{i.e.} \quad \frac{\mathrm{d}}{\mathrm{d}u}\Big[(u-u_\infty)^2\,G(u)\Big]_{u=u_\infty} = 0. \tag{2.10a,b}$$

Making use of the logarithmic derivative in (2.10) yields

$$\mathrm{i}\,\frac{a+\mathrm{i}b}{ab} - \frac{2(a+\mathrm{i}b)}{(a+\mathrm{i}b)^2-1} + \frac{4[a+\mathrm{i}(b+d)]}{[a+\mathrm{i}(b+d)]^2-c^2} + \frac{2}{a+\mathrm{i}(b+k)} = 0. \tag{2.11}$$

At this stage, all physically grounded conditions have been used, but to determine the five parameters a, b, c, d and k, we have only four real equations, which can be derived by calculating real and imaginary parts of (2.8) and (2.11). This is just the uncertainty mentioned in the Introduction, inherent to the re-entrant jet cavity model.

Let us assume that the angle β, which defines the direction of the re-entrant jet, is given. Then we infer from (2.3) that $F(1) = \mathrm{e}^{-\mathrm{i}(\alpha+\beta)}$, or

$$\frac{(1-\mathrm{i}k)(1-c-\mathrm{i}d)(1+c-\mathrm{i}d)}{(1+\mathrm{i}k)(1-c+\mathrm{i}d)(1+c+\mathrm{i}d)} - \mathrm{e}^{-\mathrm{i}(\alpha+\beta)} = 0. \tag{2.12}$$

In spite of the fact that (2.12) is written in complex form, it gives only one real-valued equation because the moduli of both terms in (2.12) equal unity identically.

Thus, from the relationships (2.8), (2.11) and (2.12), we can derive five real-valued equations for finding five accessory parameters a, b, c, d and k. The sixth parameter is $l_0 = l/J$, where J is determined in (2.7).

The algorithm for solving the system (2.8), (2.11) and (2.12) is presented in the file Algorithm.pdf stored in the supplementary materials available at https://doi.org/10.1017/jfm.2022.25.

Let N be the normal force acting on the plate, and let M be the moment about the trailing edge B. The positive direction of the moment M is anticlockwise. We introduce the following hydrodynamic coefficients:

$$C_N = \frac{2N}{\rho v_\infty^2 l}, \quad C_L = \frac{2L}{\rho v_\infty^2 l}, \quad C_D = \frac{2D}{\rho v_\infty^2 l}, \quad C_M = \frac{2M}{\rho v_\infty^2 l^2}. \tag{2.13a–d}$$

Let r be the distance between the centre of pressure on the plate and the trailing edge B. Since we calculate the moment about the trailing edge, the formula for r takes the form $r/l = -C_M/C_N$.

We denote by L_c the length of the cavity defined as the distance between the extreme left and right vertical lines that touch the cavity surface. Analogously, H_c is the width of the cavity defined as the distance between the extreme above and below horizonal lines that touch the same surface. Thus L_c and H_c determine the minimal rectangle in which it is possible to inscribe the plate–cavity system, located on the main sheet of the flow region.

For all hydrodynamic coefficients defined by formulae (2.13) as well as for dimensionless geometric characteristics δ/l, r/l, L_c/l and H_c/l, we have deduced exact analytical formulae in terms of elementary functions of the accessory parameters a, b, c, d and k. An integral-free formula has also been derived for the dimensionless conformal mapping $z(t)/l$. The derivations are also presented in the file Algorithm.pdf of Supplementary materials.

3. On the direction of the re-entrant jet

In the system of (2.8), (2.11) and (2.12), the parameter β, which defines the direction of the re-entrant, can be specified arbitrarily. In § 1, we put forward the heuristic criterion for determining β, namely, $\beta = \beta_{opt}$, where β_{opt} is the direction of the re-entrant jet that provides the minimum of the average kinetic energy of the remote part of the jet. Consider any remote part of the re-entrant jet between two sections I and II, perpendicular to the boundaries of the jet (as shown in figure 1a). Let the distance between the sections be λ. Then the kinetic flow energy of this part is $\rho v_0^2 \delta\lambda/2$, where δ is the width of the jet. The average kinetic energy per unit length is $K = \rho v_0^2 \delta/2$.

According to (1.2), $v_0 = v_\infty/\sqrt{1+\sigma}$, thus at fixed v_∞ and σ, the principle is equivalent to minimizing the function $\delta(\beta)$. First, we present simple reasoning from which it follows immediately that the angle β_{opt} always exists and $\beta_{opt} \approx \pi$. It is well known that if the cavity number is small enough, then all potential cavity models, independently of a method of organizing the flow in the cavity closure region, give similar results for integral properties. The choice of the direction of the re-entrant jet can be considered as one of such methods. Therefore, the drag forces calculated at different β must be approximately identical.

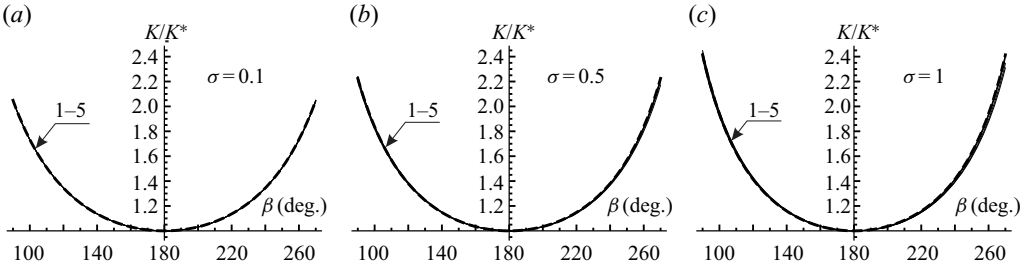

Figure 2. The dependencies of K/K^* on β. Curves 1–5 are plotted for $\alpha = 1^\circ, 10^\circ, 30^\circ, 60^\circ, 90^\circ$; dashed lines are obtained from the approximate analytical formula (3.2).

Let us denote by an asterisk the hydrodynamic properties calculated at $\beta = \pi$. Then, as follows from (1.1) and (1.2),

$$D = \delta\rho v_\infty^2\left[\sqrt{1+\sigma} - (1+\sigma)\cos\beta\right], \quad D^* = \delta^*\rho v_\infty^2\left(\sqrt{1+\sigma} + 1 + \sigma\right), \quad D \approx D^*. \tag{3.1a–c}$$

This gives

$$\frac{K}{K^*} = \frac{\delta}{\delta^*} \approx \frac{1+\sqrt{1+\sigma}}{1-\sqrt{1+\sigma}\cos\beta}. \tag{3.2}$$

Equation (3.2) yields immediately that $\beta_{opt} = \pi$, i.e. the direction of the re-entrant jet is opposite to the incident flow. Let us now check this conclusion numerically.

Consider the graphs shown in figure 2. These graphs are the dependencies of the ratio $K/K^* = \delta/\delta^*$ on the inclination angle β for five fixed angles of attack $\alpha = 1^\circ, 10^\circ, 30^\circ, 60^\circ, 90^\circ$ and three fixed cavity numbers $\sigma = 0.1, 0.5, 1$. The graphs demonstrate the existence of explicit minima that are located approximately at $\beta = 180^\circ$. Moreover, the dependencies are practically independent of the angle of attack α.

In figure 2, the results of the computations by the approximate formula (3.2) are shown by the dashed lines. The coincidence between numerical and approximate analytical results looks surprisingly good for any α and σ. It is to be noted that (3.1c), from which (3.2) follows, is approximately correct for curved plates of any shape. So at a fixed cavity number σ and any curved plate, the dependence of K/K^* on β must be approximately universal, and the minimum of K/K^* will always be attained at $\beta \approx \pi$.

In table 1, the values of β_{opt} for different α and σ are presented. The table reveals that β_{opt} is not exactly equal to π, but in the range of cavity numbers $\sigma \in (0, 1]$, the difference between $\beta = 180^\circ$ and $\beta = \beta_{opt}$ is less or slightly higher than one degree.

According to the data of table 1, the maximal difference between $\beta = \beta_{opt}$ and $\beta = 180^\circ$ is attained at $\alpha = 20^\circ$ and $\sigma = 1$. In figure 3, we have plotted together the cavity shapes at $\beta = \pi$ (solid lines) and $\beta = \beta_{opt} = 181.194^\circ$ (dashed lines) for these values of α and σ. Graphically, the results are almost indistinguishable. We have the same result for all angles of attack in the range of $\sigma \in (0.1]$. Moreover, the hydrodynamic properties, such as the lift, drag and moment coefficients, computed at $\beta = \beta_{opt}$ and $\beta = \pi$, agree at least up to four decimal places. These facts allow us to use in almost all further computations the conjecture made in the books by Gurevich (1979) and Terentiev *et al.* (2011) that states that the direction of the re-entrant jet is opposite to the incident flow.

					α (deg.)				
σ	0.1	1	5	10	20	30	45	60	90
0.1	179.954	180.065	180.145	180.08	180.036	180.021	180.011	180.006	180.0
0.2	179.946	179.954	180.34	180.26	180.133	180.079	180.041	180.022	180.0
0.3	179.945	179.875	180.428	180.455	180.268	180.165	180.088	180.048	180.0
0.4	179.947	179.825	180.429	180.615	180.421	180.27	180.147	180.08	180.0
0.5	179.95	179.794	180.385	180.729	180.579	180.386	180.215	180.118	180.0
0.6	179.953	179.775	180.321	180.798	180.73	180.509	180.291	180.161	180.0
0.7	179.957	179.765	180.251	180.832	180.869	180.634	180.371	180.208	180.0
0.8	179.961	179.76	180.182	180.839	180.994	180.756	180.454	180.257	180.0
0.9	179.965	179.759	180.117	180.826	181.102	180.875	180.539	180.308	180.0
1.0	179.969	179.761	180.058	180.8	181.194	180.988	180.623	180.36	180.0

Table 1. The values of β_{opt} for different α and σ.

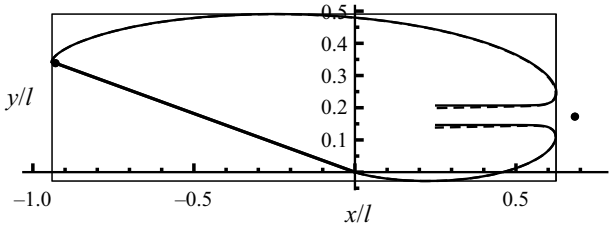

Figure 3. The plate and the cavity shape at $\alpha = 20^\circ$ and $\sigma = 1$. The solid and dashed lines are plotted for $\beta = \pi$ and $\beta = \beta_{opt} = 181.194^\circ$, respectively. The left and right disks show the stagnation points.

4. 'Abnormal' range of angle of attack

In figure 4(*a*), we show the dependencies of the lift coefficient C_L on the angle of attack α for different fixed cavity numbers σ. The graphs have been constructed in the range of angles of attack $0 \leq \alpha \in \leq 90^\circ$ for the fixed cavity numbers σ that change from 0.1 to unity with a step of 0.1. We should remark that we are not able to solve the system of (2.8), (2.11) and (2.12) at $\alpha = 0$, but for any $\alpha > 0$, the solution can be obtained. For example, we were able to carry out the computations at $\alpha = 10^{-10\circ}$.

Inspecting the graphs of figure 4(*a*), one can notice that at any fixed cavity number σ, each graph of the figure has a local minimum at a certain point $\alpha = \alpha_1$, and a local maximum at a certain point $\alpha = \alpha_2 > \alpha_1$. So at $\alpha \in (0, \alpha_1)$, we have an abnormal behaviour of the lift force L, which increases as α decreases, i.e. $\mathrm{d}C_L/\mathrm{d}\alpha < 0$. It is well known that in the cavity closure region, the flow is essentially unsteady. If the cavity length is long enough, then the influence of this unsteadiness can be neglected, and all steady potential cavity models produce similar results, which are in satisfactory agreement with experiments. According to Brennen (1995, § 8.8), for small angles of attack α, the cases $\mathrm{d}C_L/\mathrm{d}\alpha < 0$ are physically impossible due to unsteady oscillations of the cavity. On the basis of the linearized theory applied to the flat plates, Brennen demonstrated that for supercavitation, $\mathrm{d}C_L/\mathrm{d}\alpha < 0$ when $1 < L_c/l < 4/3$, where L_c is the length of the cavity. So the Brennen criterion of unsteady supercavitation is $L_c/l \leq 4/3$. Analysing experiments carried out for a circular segment of width 6.9 %, Wade & Acosta (1966) put forward an analogous criterion for the unsteadiness of supercavitating flows: $L_c/l \leq 1.2$ (see also Wade 1964). In figure 4, the points of local minima of the function $C_L(\alpha)$ at $\alpha = \alpha_1$ are marked by circles, and those where $L_c/l = 1.2$ are labelled by disks. So,

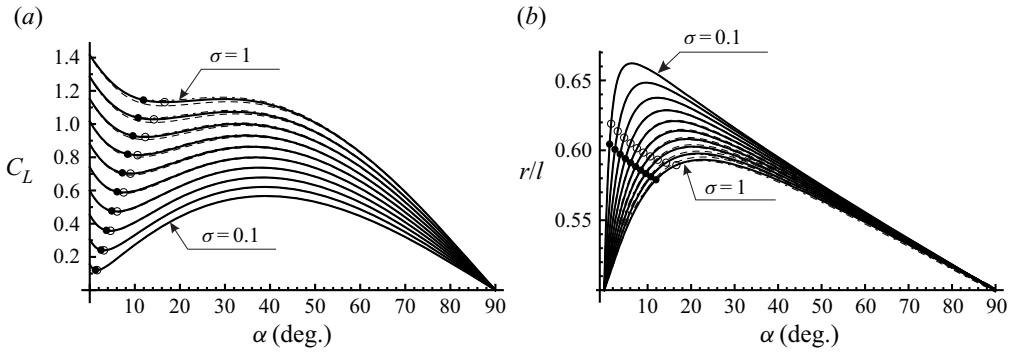

Figure 4. (*a*) The dependencies of the lift coefficient C_L on the angle of attack α. (*b*) The dimensionless distance r/l from the centre of pressure to the trailing edge B versus α. The graphs are constructed at fixed cavity numbers σ that change from 0.1 to unity with a step of 0.1. The circles mark the points of local minima of the function $C_L(\alpha)$ at $\alpha = \alpha_1$; the disks label the points for which $L_c/l = 1.2$ at $\alpha = \alpha_0$. Solid lines are constructed for $\beta = \pi$; dashed and dash-and-dot lines are constricted for $\beta = 5\pi/3$ and $2\pi/3$, respectively.

σ	$C_L(\alpha \to 0)$	α_0	$C_L(\alpha_0)$	α_1	$C_L(\alpha_1)$	$L_c(\alpha_1)/l$	α_2	$C_L(\alpha_2)$
0.1	0.154941	1.26013	0.121468	1.60519	0.12036	1.32527	39.1375	0.566634
0.2	0.30597	2.48782	0.241485	3.12673	0.23956	1.31737	38.8063	0.621315
0.3	0.453556	3.69272	0.360001	4.60315	0.3574	1.31283	38.3009	0.678248
0.4	0.598077	4.88138	0.47701	6.06052	0.473777	1.31088	37.6407	0.737509
0.5	0.739848	6.05882	0.592477	7.52547	0.588566	1.31161	36.8332	0.7992
0.6	0.87913	7.22921	0.706358	9.02822	0.701633	1.31545	35.8744	0.863448
0.7	1.01615	8.39626	0.8186	10.6061	0.812811	1.32312	34.7471	0.930424
0.8	1.15109	9.56344	0.929134	12.3133	0.921874	1.33601	33.4128	1.00036
0.9	1.28412	10.7341	1.03788	14.2436	1.02849	1.35706	31.7905	1.07361
1.0	1.41538	11.9116	1.14474	16.6084	1.1321	1.39388	29.679	1.15073

Table 2. The values characterizing the behaviour of the function $C_L(\alpha)$ at different fixed σ.

according to Brennen (1995) or Wade & Acosta (1966), the parts of the graphs in figure 4 that are to the left of the circles or disks are non-realistic and have only a theoretical meaning.

Let us denote by α_0 the angle of attack at which $L_c/l = 1.2$. In table 2, we present the values that characterize the behaviour of the functions $C_L(\alpha)$ at different fixed cavity numbers σ. It is clear that, theoretically, the maximum lift coefficient satisfies

$$C_{L\,max} = \max[C_L(\alpha \to 0), C_L(\alpha_2)]. \tag{4.1}$$

As follows from table 2, at small cavity numbers, the range $[0, \alpha_1]$ is also small but always exists. With increase of the cavity numbers, this range becomes larger, and for $\sigma \geq 0.6$, the value of C_L as $\alpha \to 0$ is maximal for the whole curve. It is interesting to note that according to table 2, $L_c/l \approx 4/3 \approx 1.33$ at $\alpha = \alpha_1$, as was predicted by Brennen (1995) with the help of the linear theory.

In figure 4(*b*), graphs analogous to those in figure 4(*a*) are plotted for the dimensionless distance r/l from the centre of pressure to the trailing edge B. Here we observe that as $\alpha \to \pi/2$, the centre of pressure tends to the middle of the plate ($r/l \to 1/2$), which is not surprising due to the symmetry with respect to the x-axis, but we have the same as $\alpha \to 0$, which is rather unexpected. Graphs analogous to those shown in figure 4 were

constructed in the monograph by Terentiev *et al.* (2011, p. 44) for the Tulin single spiral vortex model, but the authors did not investigate the limiting passage $\alpha \to 0$.

As one can see from the behaviour of the dashed and dash-and-dot lines in figure 4, the graphs of integral hydrodynamic properties plotted at $\beta = \pi, 5\pi/3, 2\pi/3$ are almost indistinguishable. Thus the conjecture of minimum kinetic energy of the re-entrant jet made in § 1 removes the uncertainty inherent to the re-entrant jet model but cannot improve the results of comparison either with experiments or with computations by RANSE methods. At the same time, it is to be noted that the abnormal range of angles of attack exists independently of the values of β.

5. Numerical investigation of the limiting passage $\alpha \to 0$

The results of the previous section demonstrate that in the framework of the potential re-entrant jet cavity model, for any cavity number $\sigma > 0$, there exists a range of angles attack $\alpha \in (0, \alpha_1)$ in which the lift coefficient C_L increases as α decreases. Hence at $\alpha \in (0, \alpha_1)$, the maximum lift coefficient C_L is attained as $\alpha = 0$. Before rejecting this 'abnormal' range of α as unrealistic, one has yet to understand the reasons for its appearance.

Consider figure 5, where the shapes of the cavities for four small angles of attack $\alpha = 2^\circ$, 1°, 0.5° and 0.05° at the cavity number $\sigma = 0.6$ are shown. As one can see, at $\alpha \leq 2^\circ$, the cavity closure region becomes close to the trailing edge B. With decrease of angles of attack, the width δ of the re-entrant almost vanishes, and the cavity tends to be symmetric with respect to the axis that is perpendicular to the plate surface and goes through the middle of the plate. This symmetry explains why $r/l \to 1/2$ as $\alpha \to 0$. Figures 5(*e–h*) demonstrate the cavity closure regions including the cavity shapes and the shapes of dividing streamlines. A surprising fact is that at $\alpha = 0.05^\circ$, the inner stagnation point migrates downwards and locates lower than the x-axis.

In figure 6, the distributions of the pressure coefficient

$$C_p = \frac{p - p_0}{\rho v_\infty^2/2} \tag{5.1}$$

are presented for the same cavity number, $\sigma = 0.6$, as in figure 5, at angles of attack $\alpha = 8^\circ, 5^\circ, 2^\circ, 1^\circ, 0.5^\circ, 0.05^\circ$ (curves 1–6). All these α are from the 'abnormal' range of angles of attack $\alpha \in (0, \alpha_1]$. Curves 3–6 in figure 6 correspond to figures 5(*e–h*). Figures 5 and 6 explain the increase of C_N and C_L with decrease of α. Indeed, in the 'abnormal' range, the inner stagnation point C in the cavity closure region locates very closely to the trailing edge B. Since at the stagnation point C the pressure achieves its maximum, this maximum influences the pressure distribution near the trailing edge, and the normal force increases together with the lift as the stagnation point approaches the trailing edge.

Let us continue to diminish the angles of attack (see figure 7). In the scale of the length l, the full cavity shapes for $\alpha < 0.05^\circ$, are almost indistinguishable from that in figure 5 at $\alpha = 0.05^\circ$. So for $\alpha < 0.05^\circ$, we have plotted in figure 7 only the cavity closure regions. The arrows indicates the direction of the flow, abbreviations RJ and DSL mean 're-entrant jet' and 'dividing streamline', respectively.

At $\alpha = 0.03^\circ$, the inner stagnation point is very close to the lower side of the plate. At $\alpha = \alpha_{crit} = 0.0293412^\circ$, the stagnation point locates directly on the lower plate surface (see figure 7*b*). Mathematically, this means that the accessory parameter is $c = 0$. The angles of attack at which $c = 0$ we shall call critical and denote by α_{crit}. At $\beta = \pi$, the

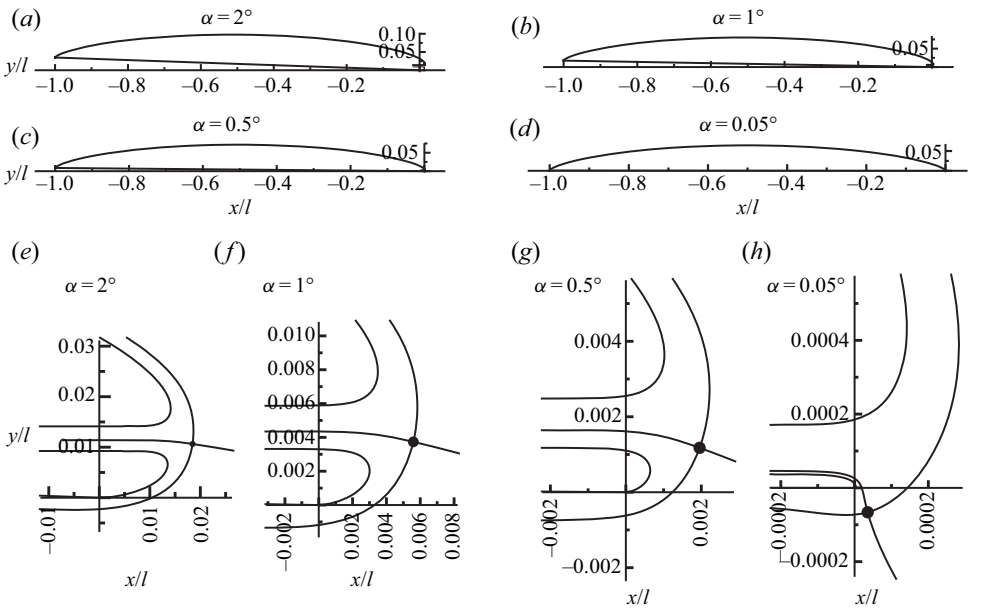

Figure 5. The shapes of the plate and cavities at $\beta = \pi$, $\sigma = 0.6$, and different small angles of attack α. Panels (*e–h*) show the corresponding cavity closure regions.

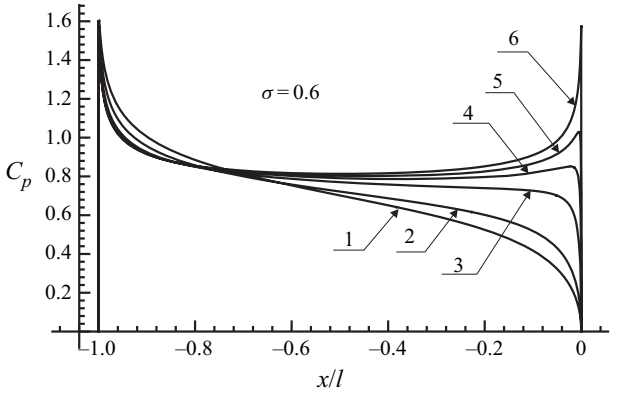

Figure 6. The distribution of the pressure coefficient C_p, determined by (5.1), at $\sigma = 0.6$ and $\alpha = 8°, 5°, 2°, 1°, 0.5°, 0, 05°$ (curves 1–6). The x-axis is directed along the plate.

angle α_{crit} depends only on the cavity number σ. In table 3, we present the angles α_{crit} for several values of σ, and as one can see, these angles turn out to be very small.

At $\alpha < \alpha_{crit}$, the parameter c becomes imaginary, which gives rise to two stagnation points lying directly on the lower side of the plate (see figure 7*c*, $\alpha = 0.027°$). In the parametric t-plane, the images of these points are $u_{01} = c + \mathrm{i}d$ and $u_{02} = -c + \mathrm{i}d$, and because c is imaginary, both images lie on the imaginary axis η. Nevertheless, all equations that have been deduced earlier remain correct, although one should take into account that in (2.1) and (2.3), $u_0 = c + \mathrm{i}d$, but $\overline{u_0} = c - \mathrm{i}d$ (as before), in spite of the fact that c is imaginary.

For all three cavity closure regions shown in figure 7, the width δ of the re-entrant jet is less than $10^{-4}l$. It is worthwhile noting also that at $\alpha < \alpha_{crit}$ (figure 7*c*), a small segment

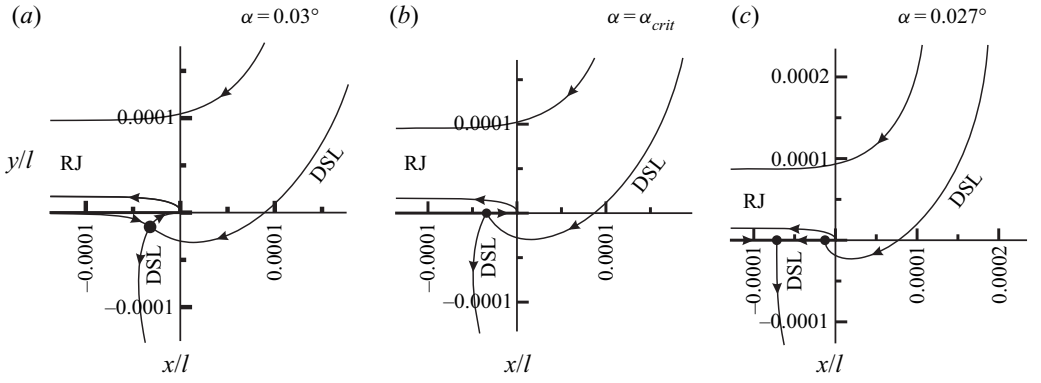

Figure 7. The cavity closure regions at $\beta = \pi$, $\sigma = 0.6$, and very small angles of attack α. The arrows indicate the directions of the velocity vectors.

σ	0.2	0.4	0.6	0.8	1.0
α_{crit}	0.00148549	0.0100785	0.0293412	0.0608145	0.105028

Table 3. Critical angles of attack versus the cavity number σ.

appears between two stagnation points on the plate surface, where the direction of the flow is opposite to the x-axis. As $\alpha \to 0$, the length of the segment increases, the width of the re-entrant jet δ tends to 0, the right stagnation point tends to the trailing edge B, and the left one shifts to the left, tending to a quite definite location. The limit is the flow that will be investigated in the next section.

6. The limiting flow configurations as $\alpha \to 0$

A sketch of the limiting flow at $\alpha = 0$ is shown in figure 8(a). The flow is symmetric with respect to the axis that is directed vertically upwards and goes through the middle of the plate. The flow has a symmetric cavity located above the plate, and two stagnation points K and C, the re-entrant jet being absent ($\delta = 0$). The incident velocity v_∞ and the cavity number σ, defined by (1.2), are assumed to be given. As the parametric domain, we choose the upper semicircle of the t-plane shown in figure 8(b). By virtue of symmetry, the images of the stagnation points K and C are m and $-m$, respectively, and the image of the point D at infinity is in, i.e. it lies on the imaginary axis. Making use of Chaplygin's method of singular points (see Gurevich 1965), we find

$$\frac{\mathrm{d}w}{\mathrm{d}t} = l_0 v_0 f(t), \quad f(t) = \frac{(1-t^2)(t^2-m^2)(1-m^2t^2)}{(t^2+n^2)^2(1+n^2t^2)^2}, \tag{6.1a,b}$$

where l_0 is an unknown positive constant, which has the dimension of length.

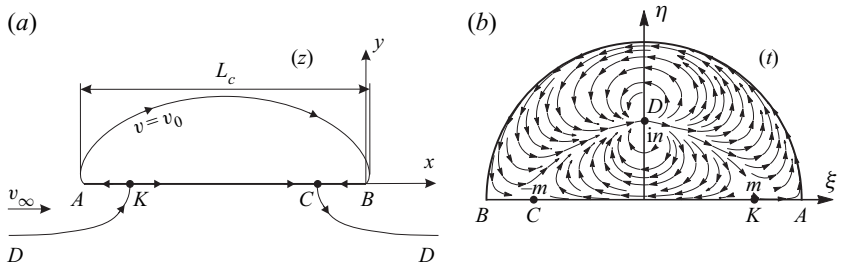

Figure 8. (*a*) Sketch of the limiting flow configuration at $\alpha = 0$. (*b*) Parametric t-plane together with streamlines.

Further, by the same method we determine

$$\frac{\mathrm{d}w}{v_0\,\mathrm{d}z} = F(t), \quad F(t) = \frac{m^2 - t^2}{1 - m^2t^2}, \tag{6.2a,b}$$

$$\frac{\mathrm{d}z}{\mathrm{d}t} = l_0\,\frac{f(t)}{F(t)} = G(t), \quad G(t) = \frac{(t^2-1)(1-m^2t^2)^2}{(t^2+n^2)^2(1+n^2t^2)^2}. \tag{6.3a,b}$$

So the problem has three unknown accessory parameters: l_0, m and n. To determine these parameters, we deduce the three equations

$$1 - 3n^2 - 3m^2n^2 + m^2n^4 = 0, \quad \frac{m^2+n^2}{1+m^2n^2} = R, \quad l = l_0\,J(m,n), \tag{6.4a–c}$$

where R is defined by (2.9), and $J = \int_{-1}^{1} G(\xi)\,\mathrm{d}\xi$. Equation (6.4*a*) follows from the closure condition $\operatorname*{res}_{t=in} G(t) = 0$, (6.4*b*) is a consequence of the relation $F(in) = R$, analogous to (2.8), and (6.4*c*) connects the length l of the plate with the parameter l_0.

The solution to the system of (6.4*a*) and (6.4*b*) is

$$m = \sqrt{\frac{(2-U)(U+1)}{(2+U)(U-1)}}, \quad n = \sqrt{\frac{U-1}{U+1}}, \quad U = \sqrt{1+\sqrt{1+\sigma}}. \tag{6.5a–c}$$

Since we have $m \geq 0$, we conclude from (6.5*a*) that $U \leq 2$ and therefore $0 < \sigma \leq 8$.

For the parameter J and the conformal mapping $z(t)$, after a little algebra, we obtain

$$J = \frac{4\mu}{n^2+1}\left(R + \frac{1}{R}\right) - \frac{4\gamma}{\pi}\tan^{-1} n, \tag{6.6}$$

where

$$\mu = \lim_{t\to in} f(t)(t-in)^2 = \frac{(1+U)^3}{2U(U^2+U-2)^2}, \tag{6.7}$$

$$\gamma = -2\pi\mathrm{i}\operatorname*{res}_{t=in} f(t) = -\frac{\pi}{2}\,\frac{(1+U)^{7/2}(U^2-2)}{(U-1)^{5/2}(U+2)^2}, \tag{6.8}$$

$$z(t) = \frac{1}{J}\,\zeta(t) - \frac{1}{2}, \quad \zeta(t) = -\frac{2\mu t}{R(t^2+n^2)} - \frac{2\mu R t}{1+n^2t^2} + \frac{4\gamma R}{\pi}\tan^{-1}(nt). \tag{6.9a,b}$$

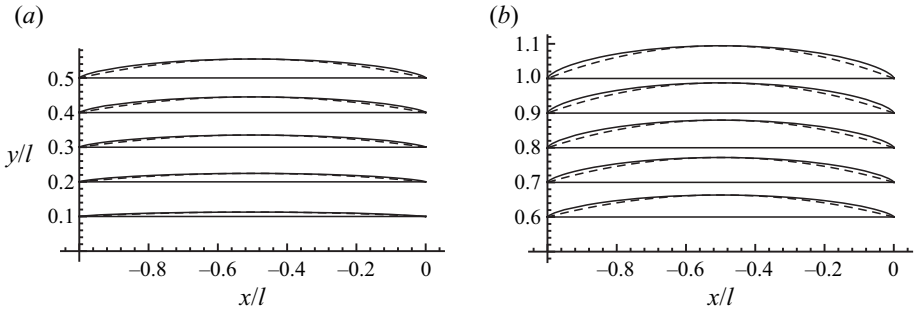

Figure 9. The shapes of the cavity bubbles for the limiting flows (solid lines). The numbers in front of the leading edges on the ordinate axis correspond to the cavity number σ. The dashed lines show the circular segments inscribed in the cavities.

The lift force N for the limiting flows over the plate is computed by the Kutta–Joukowski theorem: $N = -\rho v_\infty \Gamma$, where the circulation satisfies $\Gamma = l_0 v_0 \gamma$. Therefore,

$$C_{N\,lim} = C_{L\,lim} = -2\gamma\sqrt{1+\sigma}/J. \tag{6.10}$$

Due to d'Alembert's paradox, $C_D = 0$ for the limiting flows.

In figure 9, the shapes of the cavities for the limiting flows are presented. The number in front of the leading edges on the ordinate axis indicates the cavity number σ at which the limiting configuration has been constructed. The configurations are shifted by 0.1 with respect to each other in the vertical direction. An interesting fact is that in each of the limiting cavities, it is possible to inscribe a very simple geometric figure, namely, a circular segment of the same width h as that of the cavity. In figure 9, these segments are plotted by the dashed lines.

7. Comparison with experimental data

Dawson & Bate (1962) measured the pressure distribution on the lower side of the cavitating wedge with angle 6° at the vertex. The wedge was located in a free-surface water tunnel, and one of the investigated depths (maximal) was 2.16 model chords. Assuming that such a depth is enough to neglect the influence of the free surface, we compare the results of our computations with the experimental data by Dawson & Bate (1962). The comparison is shown in figure 10, and as one can see, the agreement looks quite satisfactory.

Wade (1964) and Wade & Acosta (1966) reported the results of the experiments for cavitating flows over a circular segment of width 6.9 %. The report by Wade (1964) contains tables with the data for C_L, C_D and the coefficients of the moment measured with respect to the middle of the plate. The data are presented for four angles of attack: $\alpha = 4°, 6°, 8°, 10°$. It is evident that

$$C_N = C_L\cos\alpha + C_D\sin\alpha, \quad C_M = C_{MW} - \tfrac{1}{2}(C_L\cos\alpha + C_D\sin\alpha), \tag{7.1a,b}$$

$$C_\tau = C_D\cos\alpha - C_L\sin\alpha, \tag{7.2}$$

where C_τ is the coefficient of the force tangential to the plate (in the ideal fluid, $C_\tau = 0$), and C_{MW} is the moment coefficient from Wade's tables taken with opposite sign, due to the mirror location (with respect to ours) of the hydrofoil and the incident flow in the

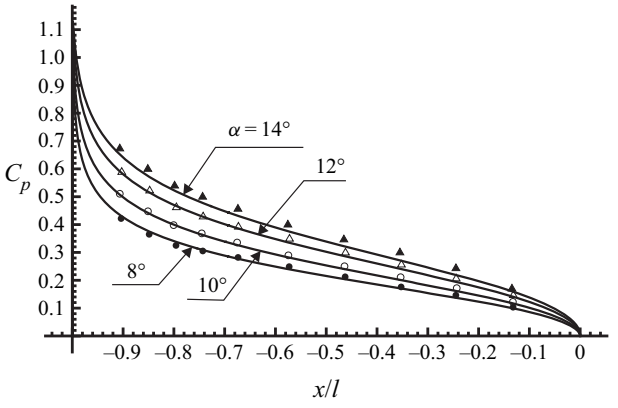

Figure 10. Distribution of the pressure coefficient C_p, determined by (5.1), at $\alpha = 8°, 10°, 12°, 14°$. The corresponding cavity numbers are $\sigma = 0.115, 0.111, 0.127, 0.12$. The x-axis is directed along the plate. The disks, circles, triangles and filled triangles are the experimental results by Dawson & Bate (1962).

experiments by Wade (1964). Thus, using (7.1) and (7.2), we have recalculated Wade's data for C_N, C_M and C_τ.

The results of the comparison are shown in figure 11. As one can see, the agreement again looks satisfactory even for cases of short cavities when $L_c/L < 1.2$, i.e. when Wade's instability criterion of the cavity is fulfilled. As can be expected, the experimental values of C_τ turn out to be small. When $L_c/L < 1.2$, these values become negative, which can be explained by the influence of the re-entrant jet.

In figure 11, the dashed lines are plotted with the help of simple analytical formulae of the linear theory presented in the paper by Geurst (1960). As one can see, this theory gives results that are very close to ours, which is not surprising because in the experiments by Wade & Acosta (1966), the angles of attack are small (from 4° to 10°).

8. Concluding remarks

In the paper, we have demonstrated that the uncertainty of the potential re-entrant jet cavity model can be fixed by minimizing the kinetic energy of the jet. Our calculations of cavity flows over oblique flat plates, based on the energy criterion, confirm the conjecture made by Terentiev *et al.* (2011) that the direction of the re-entrant jet should be opposite to the incident flow. Since for the flat plate the conclusion turns out to be correct for any angle of attack α and any cavity number $\sigma \leq 1$, we assume that the energy principle will lead to the same result for a curved plate of any shape. The approximate formula (3.2), whose deduction is independent of the plate shape, confirms this conclusion too.

An oblique flat plate is the simplest lifting shape, and the cavity flow over such a shape can be considered as a test problem for any cavity model. Another question studied in the paper is that of the limiting passage when the cavity number $\sigma > 0$ is fixed and the angle of attack α tends to zero. A natural limit of uniform flow here is impossible because the cavity number remains finite. In our opinion, such a limit gives a general characteristic of any cavity model. Let us compare the limit for the re-entrant jet model with that given by the linear theory (see Geurst 1960) for which

$$C_L = C_N = \frac{\pi\left(4\alpha^2 + \sigma^2\right)}{2\left(\sqrt{4\alpha^2 + \sigma^2} + 2\alpha\right)}, \quad C_L(\alpha \to 0) = C_{L\,lim} = \frac{\pi}{2}\sigma. \tag{8.1a,b}$$

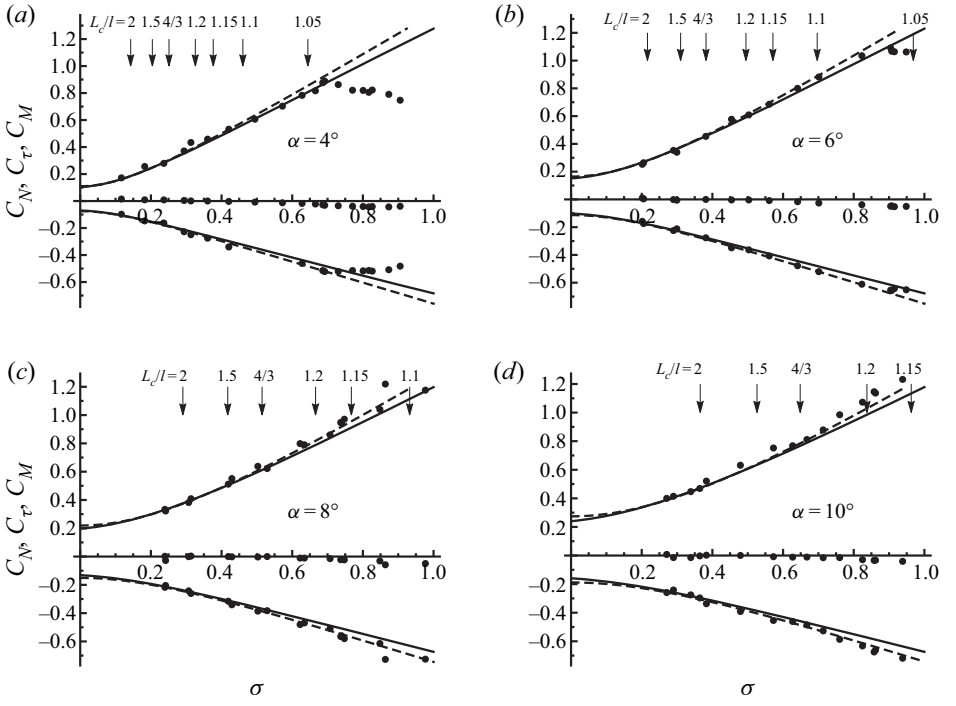

Figure 11. Solid lines are the graphs of $C_N(\sigma)$ (positive values) and $C_M(\sigma)$ (negative values). Disks are the results of Wade (1964) recalculated by formulae (7.1*a*,*b*). The disks close to the σ-axes are the results for the coefficients C_τ of the tangential force. The arrows together with the figures above them indicate the cavity numbers σ at which the corresponding L_c/l are attained. The dashed lines are obtained from formulae of the linear theory (Geurst 1960).

In the linear theory, a slight singularity at the end of the cavity occurs in a natural way from the solution of the corresponding boundary-value problem. So in the linear theory, we do not have any artificial bodies in the cavity closure region. For the re-entrant jet model, such bodies are also absent. Making use of formulae (6.5)–(6.8) and (6.10), for the limiting re-entrant jet flow, we get the expression

$$C_{L\,lim} = \frac{\pi}{2}\sigma + O(\sigma^2). \tag{8.2}$$

Comparing (8.1*b*) and (8.2), one can see that at $\alpha = 0$ and $\sigma \to 0$, the linear theory and the re-entrant jet model give the same results.

The limiting passage $\alpha \to 0$ is characterized by the following features.

(i) At small $\alpha \in (0, \alpha_1)$, the lift force L displays an abnormal behaviour: the lift coefficient C_L increases as α decreases (see figure 4 and table 2).

(ii) As $\alpha \to 0$, the width of the re-entrant jet δ and the drag coefficient C_D tend to zero, whereas the lift coefficient C_L tends to a finite and rather significant value.

(iii) The stagnation point C migrates downwards and at a certain $\alpha = \alpha_{crit}$ locates on the lower side of the plate AB very closely to the trailing edge B (see figures 5 and 7, and table 3).

(iv) An almost symmetric bubble forms above the plate, which becomes fully symmetric at $\alpha = 0$ (see figures 5 and 9).

If the stable bubble from point (iv) or something similar to it were realizable, then the large lift at small angle of attack α would be possible too. So the question is how such a bubble could be created. Our computations show that the bubble forms when the cavity length is very short ($L_c/l < 4/3$). According to Brennen (1995), this is the transition regime from steady cavity flow to cloud cavitation. Here some methods of control of the cloud cavitation can be helpful (see Kawanami *et al.* 1997; Zhang, Chen & Shao 2018).

In the literature, we have not found comparison of the results obtained by the re-entrant jet cavity model with experimental data. In § 7 of our paper, we make such a comparison and reveal good agreement.

In the supplementary materials to the paper, we store the file Algorithm.pdf, which contains the description of the algorithm for finding the accessory parameters and the deduction of pure analytical, integral-free formulae for all hydrodynamic properties. Also in these materials there are files ReentrantJet.m and ReentrantJet_Usage.nb. In the Wolfram Mathematica package ReentrantJet.m, the algorithm and formulae from Algorithm.pdf are programmed, and the notebook ReentrantJet_Usage.nb explains the usage of the package ReentrantJet.m.

Supplementary material. Supplementary material is available at https://doi.org/10.1017/jfm.2022.25.

Funding. The work was supported by the Russian Science Foundation, project no. 18-11-00115.

Declaration of interests. The authors report no conflict of interest.

Author ORCIDs.
Dmitri V. Maklakov https://orcid.org/0000-0003-0747-7082.

References

Birkhoff, G. & Zarantonello, E. 1957 *Jets, Wakes and Cavities*. Academic.

Bonfiglio, L. & Brizzolara, S. 2016 A multiphase RANSE-based computational tool for the analysis of super-cavitating hydrofoils. *Naval Engrs J.* **128** (1), 47–64.

Brennen, C.E. 1995 *Cavitation and Bubble Dynamics*. Oxford University Press.

Dawson, T.E. & Bate, E.R. 1962 An experimental investigation of a fully cavitating two-dimensional flat-plate hydrofoil near a free surface. *Tech. Rep*. E-118.12. Karman Laboratory of Fluid Mechanics and Jet Propulsion, California Institute of Technology.

DeLillo, T.K., Elcrat, A.R. & Hu, C. 2005 Computation of the Helmholtz–Kirchhoff and reentrant jet flows using Fourier series. *Appl. Maths Comput.* **163**, 397–422.

Efros, D. 1946 Hydrodynamical theory of two-dimensional flow with cavitation. *Dokl. Akad. Nauk SSSR* **51** (4), 267–270.

Franc, J.-P. & Michel, J.-M. 2004 *Fundamentals of Cavitation. Fluid Mechanics and its Applications*, vol. 76. Kluwer Academic.

Geurst, J.A. 1960 Linearized theory for fully cavitated hydrofoils. *Intl Shipbuilding Prog.* **7** (65), 17–27.

Gilbarg, D. 1960 *Jets and Cavities, Encyclopedia of Physics*, vol. 9. Springer.

Gilbarg, D. & Serrin, J. 1950 Free boundaries and jets in the theory of cavitation. *J. Maths Phys.* **29**, 1–12.

Gurevich, M.I. 1965 *The Theory of Jets in an Ideal Fluid*. Academic.

Gurevich, M.I. 1979 *The Theory of jets in an Ideal Fluid*, 2nd edn. Nauka.

Karn, A., Arndt, R.E.A. & Hong, J. 2016 An experimental investigation into supercavity closure mechanisms. *J. Fluid Mech.* **789**, 259–284.

Kawanami, Y., Kato, H., Yamaguchi, H. & Tagaya, M.T.Y. 1997 Mechanism and control of cloud cavitation. *Trans. ASME J. Fluids Engng* **119** (4), 788–794.

Kinnas, S. & Fine, N. 1991 Non-linear analysis of the flow around partially or super-cavitating hydrofoils by a potential based panel method. In *Boundary Integral Methods* (ed. L. Morino & R. Piva), pp. 289–300. Springer.

Kreisel, G. 1946 Cavitation with finite cavitation numbers. *Tech. Rep.* Rl/H/36. Admiralty Research Laboratory.

Milne-Thomson, L.M. 1968 *Theoretical Hydrodynamics*, 4th edn. Macmillan.

MIMURA, Y. 1958 The flow with wake past an oblique plate. *J. Phys. Soc. Japan* **13** (9), 1048–1055.
NIEDZWIEDZKA, A., SCHNERR, G.H. & SOBIESKI, W. 2016 Review of numerical models of cavitating flows with the use of the homogeneous approach. *Arch. Thermodyn.* **37** (2), 71–88.
PALATINI, A. 1916 Sulla confluenza di due vene. *Atti del R. Istituto Veneto di Sc. Lett. ed Arti* **LXXV** (parte 2), 451–463.
TERENT'EV, A.G. 1976 Nonlinear theory of cavitational flow around obstacles. *Fluid Dyn.* **11**, 142–145.
TERENTIEV, A.G., KIRSCHNER, I.N. & UHLMAN, J.S. 2011 *The Hydrodynamics of Cavitating Flows*. Backbone.
TULIN, M.P. 1964 Supercavitating flows – small perturbation theory. *J. Ship Res.* **7** (3), 16–36.
VERNENGO, G., BONFIGLIO, L., GAGGERO, S. & BRIZZOLARA, S. 2016 Physics-based design by optimization of unconventional supercavitating hydrofoils. *J. Ship Res.* **60** (4), 187–202.
WADE, R.B. 1964 Water tunnel observations on the flow past plano-convex hydrofoil. *Tech. Rep.* E-79.6. Hydrodynamics Laboratory, California Institute of Technology.
WADE, R.B. & ACOSTA, A.J. 1966 Experimental observations on the flow past a plano-convex hydrofoil. *Trans. ASME J. Basic Engng* **88**, 273–283.
WU, T.Y.-T. 1956 A free streamline theory for two-dimensional fully cavitated hydrofoils. *Stud. Appl. Maths* **35** (1–4), 236–265.
WU, T.Y.-T. 1962 A wake model for free-streamline flow theory. Part 1. Fully and partially developed wake flows and cavity flows past an oblique flat plate. *J. Fluid Mech.* **13** (2), 161–181.
ZHANG, L., CHEN, M. & SHAO, X. 2018 Inhibition of cloud cavitation on a flat hydrofoil through the placement of an obstacle. *Ocean Engng* **155**, 1–9.